PNAS Nexus, 2024, 3, pgae208
https://doi.org/10.1093/pnasnexus/pgae208
Advance access publication 27 May 2024
Research Report

Accurate and rapid molecular subgrouping of high-grade glioma via deep learning-assisted label-free fiber-optic Raman spectroscopy

Chang Liu [a,1], Jiejun Wang [b,1], Jianghao Shen [a,1], Xun Chen [a,c,*], Nan Ji [b,*] and Shuhua Yue [a,*]

[a]Key Laboratory of Biomechanics and Mechanobiology (Beihang University), Ministry of Education, Institute of Medical Photonics, Beijing Advanced Innovation Center for Biomedical Engineering, School of Biological Science and Medical Engineering, Beihang University, Xueyuan Road 37, Beijing 100191, China
[b]Department of Neurosurgery, Beijing Tiantan Hospital, Capital Medical University, South Fourth Ring West Road 119, Beijing 100050, China
[c]School of Engineering Medicine, Beihang University, Xueyuan Road 37, Beijing 100191, China
*To whom correspondence should be addressed: Email: chenxun2007@buaa.edu.cn (X.C.); Email: jinan@mail.ccmu.edu.cn (N.J.); Email: yue_shuhua@buaa.edu.cn (S.Y.)
[1]C.L., J.W., and J.S. authors contributed equally to this work.
Edited By: Josh Wand

Abstract

Molecular genetics is highly related with prognosis of high-grade glioma. Accordingly, the latest WHO guideline recommends that molecular subgroups of the genes, including IDH, 1p/19q, MGMT, TERT, EGFR, Chromosome 7/10, CDKN2A/B, need to be detected to better classify glioma and guide surgery and treatment. Unfortunately, there is no preoperative or intraoperative technology available for accurate and comprehensive molecular subgrouping of glioma. Here, we develop a deep learning-assisted fiber-optic Raman diagnostic platform for accurate and rapid molecular subgrouping of high-grade glioma. Specifically, a total of 2,354 fingerprint Raman spectra was obtained from 743 tissue sites (astrocytoma: 151; oligodendroglioma: 150; glioblastoma (GBM): 442) of 44 high-grade glioma patients. The convolutional neural networks (ResNet) model was then established and optimized for molecular subgrouping. The mean area under receiver operating characteristic curves (AUC) for identifying the molecular subgroups of high-grade glioma reached 0.904, with mean sensitivity of 83.3%, mean specificity of 85.0%, mean accuracy of 83.3%, and mean time expense of 10.6 s. The diagnosis performance using ResNet model was shown to be superior to PCA-SVM and UMAP models, suggesting that high dimensional information from Raman spectra would be helpful. In addition, for the molecular subgroups of GBM, the mean AUC reached 0.932, with mean sensitivity of 87.8%, mean specificity of 83.6%, and mean accuracy of 84.1%. Furthermore, according to saliency maps, the specific Raman features corresponding to tumor-associated biomolecules (e.g. nucleic acid, tyrosine, tryptophan, cholesteryl ester, fatty acid, and collagen) were found to contribute to the accurate molecular subgrouping. Collectively, this study opens up new opportunities for accurate and rapid molecular subgrouping of high-grade glioma, which would assist optimal surgical resection and instant post-operative decision-making.

Introduction

High-grade gliomas are the most common and aggressive primary tumors of the central nervous system (1). An increasing evidence has indicated that molecular genetics profoundly affect prognostic implications of high-grade glioma (2). Accordingly, the latest edition of the World Health Organization Classification of Tumors of the Central Nervous System (WHO CNS5) recommends to integrate molecular subgrouping of the genes, including IDH, 1p/19q, MGMT, TERT, EGFR, Chromosome 7/10, CDKN2A/B, and traditional histological features together to gain a more clinically relevant classification, which thereby can guide surgery with optimal extent of resection and instant post-operative therapy (3–5).

Nevertheless, the current techniques for molecular subgrouping by using surgically removed specimens, including next-generation sequencing, immunohistochemistry, and cytogenetic testing (6), are too time-consuming to provide timely diagnostic results during surgery. Recent advances in magnetic resonance imaging (MRI) have demonstrated preoperative molecular subgrouping of IDH mutation (7), 1p/19q codeletion (8), and MGMT methylation (9) with area under receiver operating characteristic curves (AUC) > 0.8. Unfortunately, such method so far still lacks sufficient and rational biological explanation, which hinders reliable diagnosis (7, 9, 10). Moreover, molecular subgroups regarding TERT, EGFR, Chromosome 7/10, and CDKN2A/B have not yet been investigated by MRI (11, 12). Thus, there is an urgent clinical need for accurate, rapid, comprehensive detection of multiple molecular subgroups simultaneously.

Raman spectroscopy, a label-free optical vibrational spectroscopy technique, has been widely used to quantitatively analyze molecular compositions of biological specimens and diagnosis of various human cancers (13–21). AI algorithms have been shown to improve the robustness of Raman spectroscopy-based precise

Competing Interest: The authors declare no competing interest.
Received: December 14, 2023. **Accepted:** May 17, 2024

cancer diagnosis (22). Particularly, previous studies have demonstrated the capability of Raman spectroscopy in intraoperative brain cancer detection (23–27). Regarding molecular subgrouping, most Raman spectroscopy studies focused on detection of IDH mutation, the accuracy of which ranged from 80 to 90% (28–30). Unfortunately, other molecular subgroups regarding MGMT, TERT, EGFR, Chromosome 7/10, and CDKN2/B have not been investigated using Raman spectroscopy. More recently, Hollon et al. (31) developed an artificial intelligence-assisted molecular classification specific to the genes, i.e. IDH, 1p/19q, and ATRX, of diffuse gliomas with accuracy >90%. However, this approach was developed based on laser-scanning stimulated Raman scattering microscopy, which is so far limited to the small field of view and thus difficult to cover enough tissue area in a timely manner for diagnosis.

To fulfill the unmet clinical need, here we developed a deep learning-assisted label-free fiber-optic Raman spectroscopy for accurate and rapid molecular subgrouping of high-grade glioma. Specifically, a total of 2,354 fingerprint Raman spectra were acquired from 743 tissue sites of 44 high-grade glioma patients. The convolutional neural network (ResNet) model was used for classifications. The mean AUC for identifying the molecular subgroups regarding IDH, 1p/19q, MGMT, TERT, EGFR, Chromosome 7/10, and CDKN2A/B in high-grade glioma reached 0.904, with mean sensitivity of 83.3%, mean specificity of 85.0%, mean accuracy of 83.3%, and mean time expense of 10.6 s. Compared with the performance of conventional machine learning and manifold learning, the ResNet model achieved better performance owing to its capability of extracting high-order molecular-related information in 1D spectral data. Furthermore, according to saliency maps, the specific Raman features corresponding to tumor-associated biomolecules (e.g. nucleic acid, tyrosine, tryptophan, cholesteryl ester, fatty acid, and collagen) were found to contribute to the accurate molecular subgrouping. Together, our study heralds the potential of deep learning-assisted label-free fiber-optic Raman spectroscopy for rapid and comprehensive detection of multiple molecular subgroups of high-grade glioma with accuracy beyond current capabilities.

Results

Workflow of high-grade glioma molecular subgrouping

According to WHO CNS5, our study focused on molecular subgroups regarding the genes, i.e. IDH, 1p/19q, MGMT, TERT, EGFR, Chromosome 7/10, and CDKN2A/B, of high-grade glioma (Fig. 1). As shown in Fig. 2a, the workflow of deep learning-assisted fiber-optic Raman diagnostic platform for molecular subgrouping of high-grade glioma was described. Specifically, spontaneous Raman spectra were first acquired using fiber-optic Raman spectroscopy (Fig. S1) with around 5 s for each tissue site (the details are described in the Methods section and patient information is shown in Table S1). Second, the spectra were preprocessed for auto-fluorescence removal, denoising, and min–max normalization. Third, for each molecular subgrouping task, the processed Raman spectral data were split into three datasets (90% for training and 9-fold validation and 10% for testing) for deep learning-based classification. In order to solve the problem of data imbalance, random oversampling was used in training and validation set, but not in test set. The prediction performance of the test dataset was considered as the final result of the deep learning classification model. To compare the performance between deep learning (e.g. residual network [ResNet]), machine learning (e.g. principal component analysis [PCA], support vector machine learning [SVM]) and manifold learning (e.g. uniform manifold approximation and projection [UMAP]) models, the confusion matrix and receiver operating characteristic (ROC) curve were evaluated in the test dataset. Finally, as shown in Fig. 2b, the Raman spectra were classified by using 1D ResNet with *Tanh* activation functions. To achieve accurate optimization of hyper parameters of network, backpropagation and gradient descent were used to fit spectral wavenumber information. Moreover, saliency maps were analyzed by binary stochastic filtering (BSF) to quantify the contribution level of each Raman shift for the classification. The details of model training and testing were described in the Methods section.

Raman spectral analysis of human high-grade glioma tissues

Using the fiber-optic Raman spectroscopy, we acquired a total of 2,354 spontaneous Raman spectra (fingerprint region) on 743 tissue sites (astrocytoma: 151; oligodendroglioma: 150; glioblastoma (GBM): 442) obtained from 44 high-grade glioma patients (astrocytoma: 7; oligodendroglioma: 8; GBM: 29) undergone resection. Figure 3 shows mean spectra with standard deviation after preprocessing for each molecular subgroup and the difference spectra between each paired subgroup (i.e. IDH wildtype vs. IDH mutation, 1p/19q intact vs. 1p/19q codeletion, MGMT unmethylation vs. MGMT methylation, TERT wildtype vs. TERT mutation, EGFR nonamplification vs. EGFR amplification, Chromosome +7/−10 vs. Chromosome +7/−10 Wildtype, and CDKN2A/B retention vs. CDKN2A/B homozygous deletion). In most of the difference spectra, the Raman band for CH_2 bending around 1440 cm^{-1} was consistently observed. The spectral differences for subgroups regarding 1p/19q, MGMT, TERT, and EGFR were attributed to Amide I band around 1,661 cm^{-1} (C=O stretching of protein backbone) and Amide III band between 1,200 and 1,380 cm^{-1} (C–H and N–C bending). Additional spectral difference for subgroups of IDH, 1p/19q, MGMT, TERT, Chromosome 7/10, and CDKN2A/B can be found near collagen bands at 854 and 938 cm^{-1} and lipid bands from 492 to 605 cm^{-1}.

Deep learning-assisted molecular subgrouping of high-grade glioma

We developed 1D ResNet model for molecular subgrouping based on the 2,354 spectra acquired on fiber-optic Raman system. According to the characteristics of Raman spectra, nonlinear function activation *Tanh* instead of *Relu* or *Linear* were selected in the convolutional layers of 1D ResNet. These convolution layers were able to extract molecular signatures implied in high-order information of spectral curves. The *softmax* function was used as the activation function in the output layer, which output probabilities of two classes with the higher value considered to be the predicted class. The binary classification models for each pair of subgroups were first trained and optimized with their training dataset and validation dataset, respectively. The performance of the binary models was then evaluated using the corresponding test dataset.

As shown in Fig. 4, the average AUCs of deep learning (ResNet)-based molecular subgrouping for IDH, 1p/19q, MGMT, TERT, EGFR, Chromosome 7/10, and CDKN2A/B were 0.969, 0.932, 0.893, 0.904, 0.838, 0.883, and 0.912, respectively. Figure 5a shows the heatmap of sensitivity, specificity, accuracy and AUC for molecular subgrouping of high-grade glioma. In terms of the previously most investigated molecular alterations (IDH and 1p19q), our deep learning model (ResNet) achieved

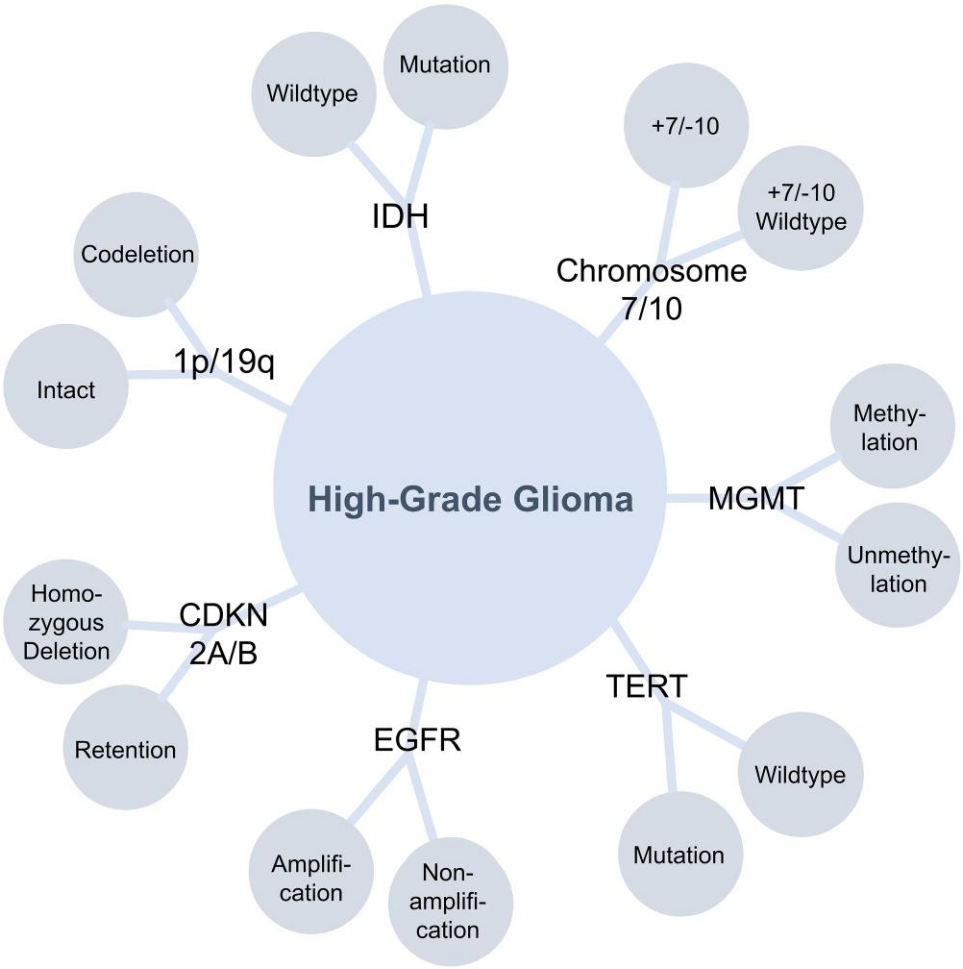

Fig. 1. Key molecular alterations of high-grade glioma. According to 2021 WHO classification system (WHO CNS5), typical molecular alterations regarding IDH, 1p/19q, MGMT, TERT, EGFR, Chromosome 7/10, and CDKN2A/B were selected for high-grade glioma subgrouping.

overall diagnostic accuracy of 90.54% (sensitivity of 93.60% and specificity of 92.68%) and 86.19% (sensitivity of 84.44% and specificity of 89.06%), respectively. For the other subgrouping (for MGMT, TERT, EGFR, Chromosome 7/10, and CDKN2A/B), the diagnostic sensitivity, specificity, accuracy, and AUC ranged from 67.08 to 91.01%, from 73.58 to 91.49%, from 78.98 to 83.29%, and from 0.838 to 0.912, respectively. The detailed confusion matrix was shown in Table S2.

To investigate whether deep learning is superior to other types of models for this application, SVM as an example of machine learning models and UMAP as an example of manifold leaning models were built. As shown in Figs. S2–S6, the detailed performance of machine learning (SVM), manifold learning (UMAP), and deep learning (ResNet), indicated that deep learning is more appropriate for classification of most molecular subgroups. Specifically, the deep learning (ResNet) achieved higher accuracy and AUC than both machine learning (SVM) and manifold learning (UMAP) for identification of all molecular subgroups. Moreover, compared with PCA-SVM and UMAP, ResNet showed higher sensitivity and specificity for subgrouping IDH, MGMT, Chromosome 7/10 and CDKN2A/B; Meanwhile, for subgrouping of 1p19q, TERT, and EGFR, manifold learning gained higher sensitivity than ResNet.

The effectiveness of our classification models in molecular subgrouping of GBMs (Fig. S7) was further demonstrated. From 422 tissue sites of 29 GBM patients, 1,694 Raman spectra are preprocessed (Fig. S8), split and fed into the training set and test set of models. Table S2 shows the sensitivity, specificity, accuracy, and AUC for molecular subgrouping of GBM, ranging from 83.33 to 91.19%, from 79.17 to 91.67%, from 80.77 to 87.61%, and from 0.888 to 0.976, respectively. The heat map in Fig. 5b compares the performance between ResNet and the other two models, demonstrating our ResNet was superior over the others for molecular subgrouping of GBMs.

To further validate the robustness of the classification algorithm, we evaluated the subgrouping performance of each model with original 44 patients and extra 10 patients. The information of extra patients was summarized in Table S3. The subgrouping accuracy and AUC in the 50 patients of each model were summarized in Table S4. The performance of deep learning did not change much in the 50 patients, preliminarily proving the robustness of molecular subgrouping. The subgrouping performance was also evaluated upon an external validation. The work flow was shown in Fig. S9. Nineteen tissue samples from a total of 92 tissues were selected as external validation dataset for evaluation of subgrouping models. The subgrouping performance evaluated in the external validation dataset was summarized in Table S5. The AUC for deep learning-based molecular subgrouping of IDH and 1p19q remained over 0.9 in the external dataset. Meanwhile, for subgrouping of IDH, UMAP gained higher accuracy

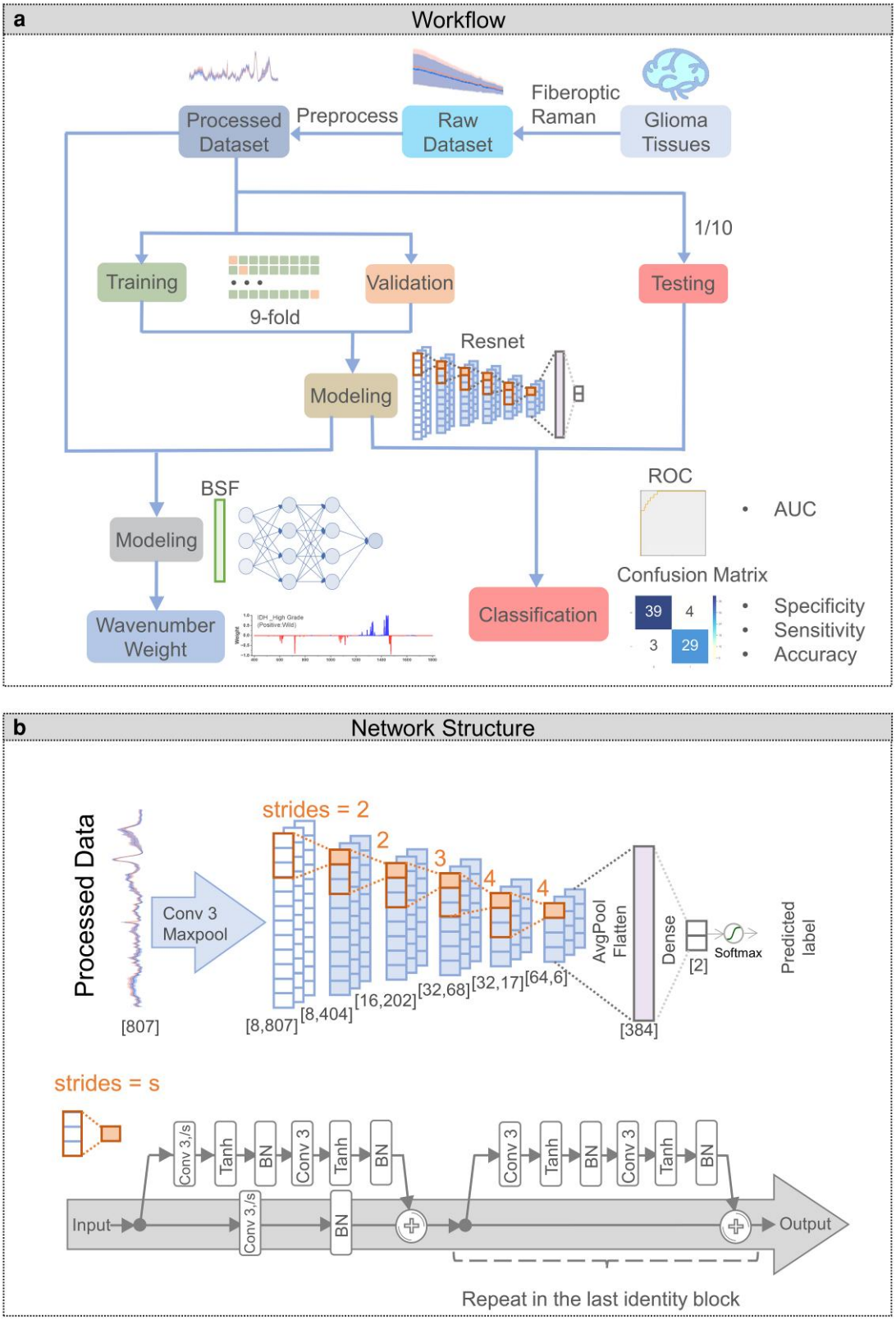

Fig. 2. Deep learning-assisted Raman subgrouping scheme for molecular alterations of high-grade glioma. a) Workflow of Raman molecular subgrouping, including dataset preparation, Resnet model training for classification and BSF model training for weighing wavenumber contribution. For each molecular subgrouping task, Raman spectral data was acquired, preprocessed and split into three datasets (90% for training and 9-fold cross validation and 10% for testing) for deep learning-based classification. The confusion matrix and receiver operating characteristic (ROC) curve were evaluated in the test dataset. A binary stochastic filtering model was optimized by the trained Resnet and the spectral data for saliency maps quantifying the contribution level of each Raman shift for the classification. AUC, area under receiver operating characteristic curves. b) Structure of the Resnet model. The numbers in bracket represent the size [(channels) length] of the hidden layers. The numbers represent the strides of the first convolution layer in each identity block (dash line). Conv, convolution layer with kernel size = 3 and strides = s, BN, batch normalization.

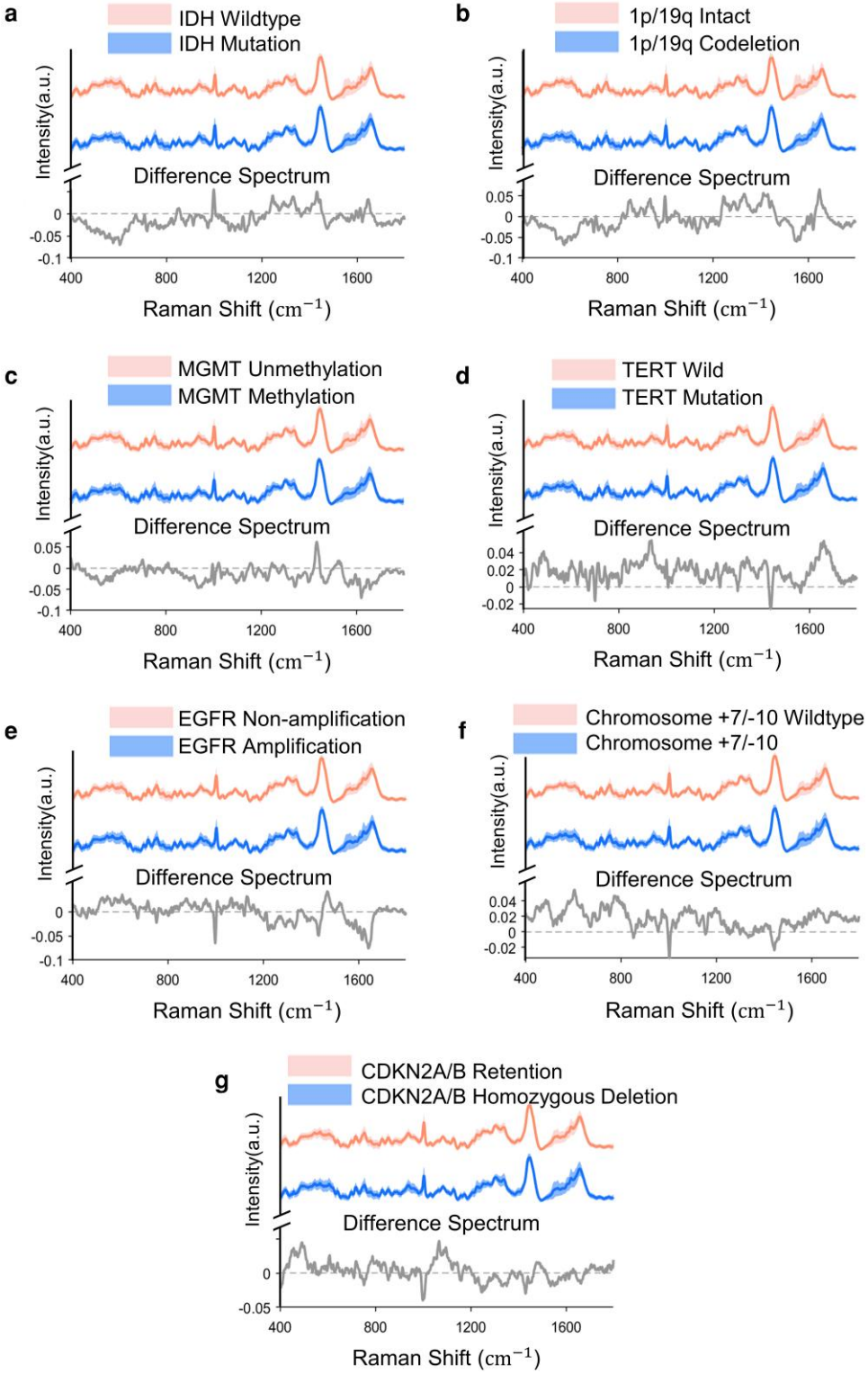

Fig. 3. Raman spectra for high-grade glioma molecular alterations with binary labels. Each panel shows average spectra of different molecular alterations with binary labels. Raman spectral differences between each pair of labels (subtract blue from red) are also plotted as difference spectra. a) IDH wild and mutation. b) 1p/19q intact and codeletion. c) MGMT unmethylation and methylation. d) TERT wildtype and mutation. e) EGFR nonamplification and amplification. f) Gain of chromosome 7 and loss of chromosome 10 (chromosome +7/−10) and wildtype. g) CDKN2A/B homozygous deletion and retention.

and AUC than Resnet, which is probably because nonlinear dimensional reduction function fits the spectral difference.

Collectively, our deep learning-assisted label-free fiber-optic Raman spectroscopy achieves better performance than previous studies in identification of IDH subgroups (28–30), and more importantly, established a new way for subgrouping of the other key molecular genetics (i.e. 1p19q, MGMT, TERT, EGFR, +7/−10, and CDKN2A/B) of high-grade glioma.

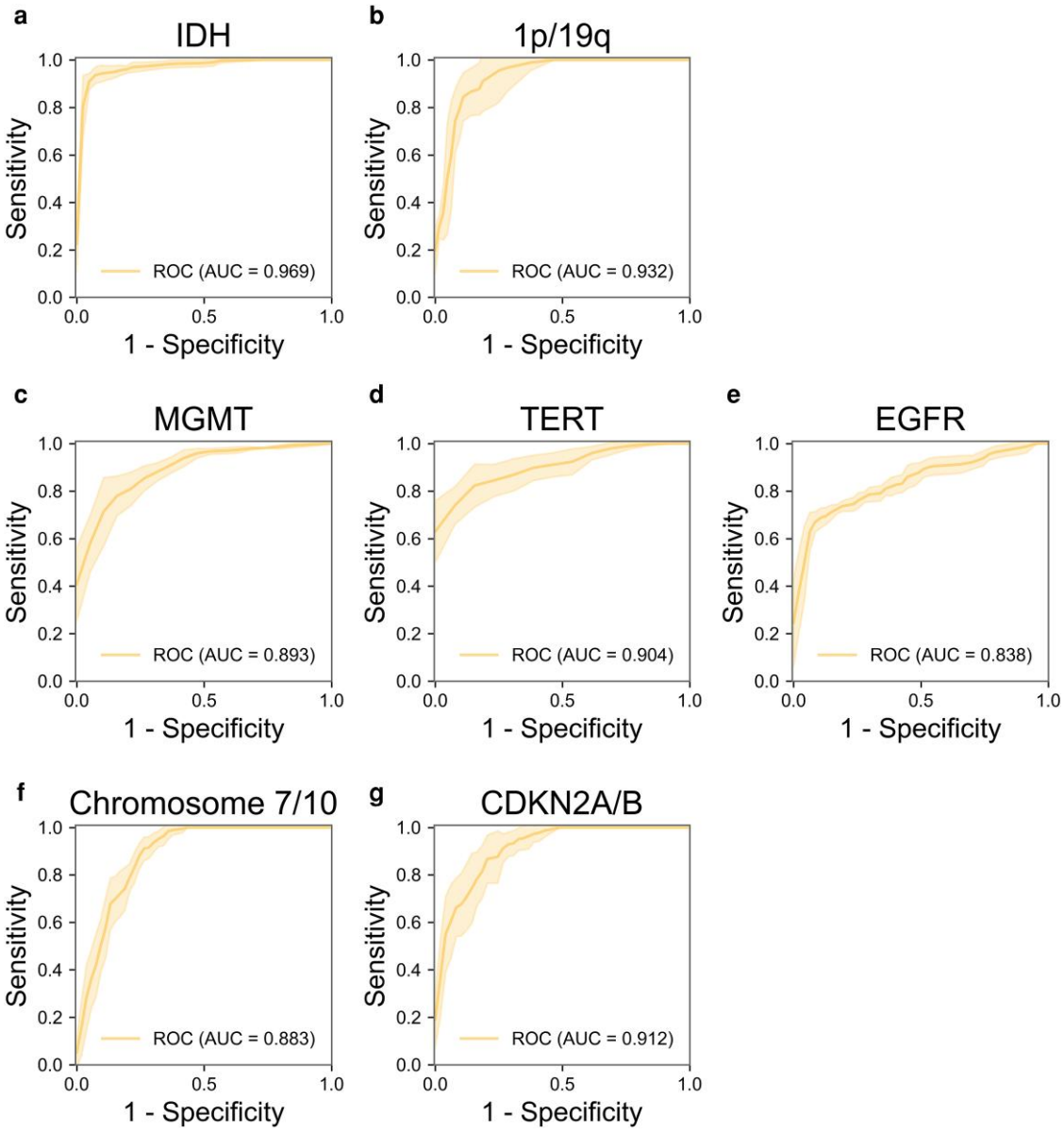

Fig. 4. Raman diagnostic ROC using deep learning (ResNet) model for molecular subgrouping of high-grade glioma. AUC, area under the curve. a) IDH mutation, b) 1p/19q codeletion, c) MGMT methylation, d) TERT mutation, e) EGFR amplification, f) Chromosome +7/−10, g) CDKN2A/B homozygous deletion.

Raman signatures for biomolecules contributing to the accurate molecular subgrouping

To further elucidate the key biomolecular information in Raman spectra contributing to the accurate molecular subgrouping based on ResNet model, we added BSF after the ResNet input and retrained it to quantify the filter layer weight parameters (32). The simulated layer weight was corresponding to the Raman shift for the diagnostic models. In our binary label classification, this weight represents the correlation between the intensity of related Raman shift and the prediction contribution of positive label, namely the importance of Raman shifts for subgrouping. The weight in each molecular alteration is plotted as Resnet determined importance in Fig. 6, followed by difference spectrum determined importance from mean spectra subtraction. The Raman shift importance determined by Resnet and difference spectra are consistent. The key Raman shifts determined by Resnet are summarized in Table S6. To determine the relationship between spectroscopic changes and biochemical changes, we referred to previous studies (33, 34) which compiled the most widely observed peak frequencies and their assignments in biological tissue.

For detection of IDH mutation in the saliency map, the positive Raman bands were corresponding to phosphatidylinositol (around 577 cm^{-1}), and phospholipid (around 1,078 cm^{-1}); meanwhile the negative Raman bands were corresponding to collagen (around 1,448 cm^{-1}) and lipid (around 1,433 cm^{-1}). It is worth noting that the decline of lipids and collagen in IDH-mutated glioma is in line with previous studies (35, 36). Mutated IDH causes α-KG (α-ketoglutarate) in the tricarboxylic acid cycle to be converted into 2-HG (2-hydroxyglutarate). High levels of 2-HG inhibit the synthesis of lipids such as triglycerides, and high levels of D2-HG (One of the stereoisomers of 2-HG) block the prolyl hydroxylation of collagen, leading to defects in collagen proteins. For detection of 1p/19q codeletion in the saliency map, the

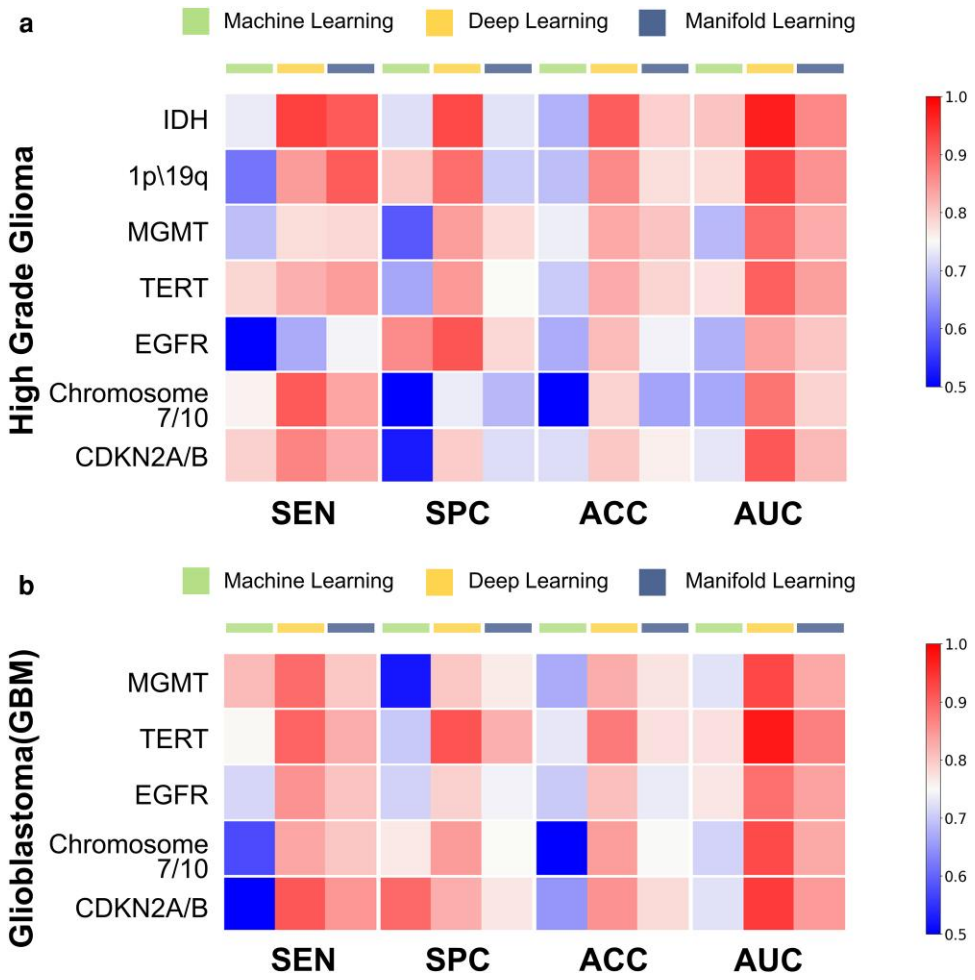

Fig. 5. Heatmap of Raman subgrouping performance based on different models. Sensitivity, specificity, accuracy and AUC of machine learning (SVM), manifold learning (UMAP), and deep learning (ResNet) models using Raman spectral datasets for subgrouping. SEN, sensitivity, SPC, specificity; ACC, accuracy; AUC, area under classification. Positive labels: IDH mutation, 1p/19q codeletion, MGMT methylation, TERT mutation, EGFR amplification, Chromosome +7/−10, and CDKN2A/B homozygous deletion. a) Diagnostic performance for High-grade glioma molecular subgrouping, b) diagnostic performance for GBM molecular subgrouping.

positive Raman bands are corresponding to amino acid (serine and cysteine, around 524 cm^{-1}), and nucleic acid (around 1,085 and 1,094 cm^{-1}). Previous research indicated that genes including phosphoglycerate dehydrogenase (PHGDH) and cystathionine gamma-lyase (CTH), situated on chromosome 1p, are linked to the pathway involved in the synthesis of serine and cystathionine (37).

In MGMT recognition in the saliency map, the positive Raman bands were corresponding to the protein (around 951 cm^{-1} and 1,560 cm^{-1}), the negative Raman bands were corresponding to fatty acids (around 1,442 cm^{-1}). The accumulation of lipids of LDs of cells in MGMT methylated glioma may be due to the down-regulated genes related to lipid efflux (38). In TERT recognition in the saliency map, the negative Raman bands were corresponding to cysteine (540 cm^{-1}). In EGFR recognition in the saliency map, the positive Raman bands were corresponding to the phenylalanine (around 1,000 cm^{-1}) and β-sheet of protein (around 1,221 cm^{-1}), while the negative Raman bands were corresponding to tyrosine (around 850 cm^{-1} and 856 cm^{-1}). A recent study indicated that in the treatment of lung adenocarcinoma patients with EGFR mutations using EGFR tyrosine kinase inhibitors (EGFR-TKI), those with drug resistance exhibited higher levels of N-acetyl-d-phenylalanine, which may indirectly suggest that EGFR mutations correspond to an increase in phenylalanine levels (39).

In Chromosome copy number +7/−10 recognition in the saliency map, the positive Raman bands were corresponding to ν(C–C) skeletal of acyl backbone in lipid (around 1,129 cm^{-1}) and stretching mode (C–C and C–N) of glycogen (around 1,155 cm^{-1}), while the negative Raman bands were corresponding to palmitic acid (around 1,068 cm^{-1}). A previous study linked specific regions on chromosome 7 to the regulation of glycogen synthesis in mouse models, which provides support for the biochemical changes brought about by the molecular alterations in chromosomes 7 and 10 (40). In CDKN2A/B recognition in the saliency map, the positive Raman bands were corresponding to tyrosine in collagen type I (around 1,169 cm^{-1}), while the negative Raman bands were corresponding to skeletal C–C stretch of lipids (around 1,064 cm^{-1}) and tryptophan (around 1,618 cm^{-1}). Researchers identified that CDKN2A-deleted GBMs show heightened levels of lipid peroxidation, as the absence of CDKN2A alters the lipid composition of these tumors (41).

Taken together, the ResNet model was able to recognize the relative intensity changes of multiple Raman bands specific to biomolecules (e.g. nucleic acid, tyrosine, tryptophan, cholesteryl ester, fatty acid, and collagen), which were strongly associated with molecular genetics of high-grade glioma.

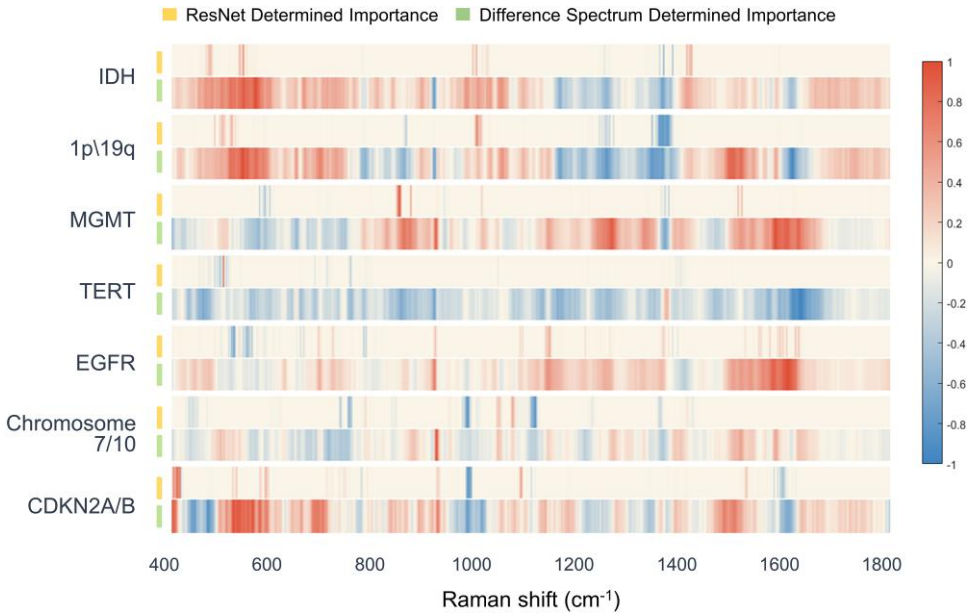

Fig. 6. Saliency maps in ResNet model for Raman shift signatures. ResNet determined importance (from BSF, represents the correlation between the intensity of related Raman shift and the prediction contribution of positive labels) and difference spectrum determined importance (from mean spectra subtraction between spectra of positive and negative labels), normalized with max values of difference spectrum. Positive labels: IDH mutation, 1p/19q codeletion, MGMT methylation, TERT mutation, EGFR amplification, Chromosome +7/−10, and CDKN2A/B homozygous deletion.

Discussion

In this work, we developed the deep learning-assisted Raman diagnostic platform for accurate and rapid molecular subgrouping of high-grade glioma and GBM. First, a total of 2,354 fingerprint Raman spectra were acquired from 743 tissue sites of 44 high-grade glioma patients. Second, our deep learning models were trained and tested. The mean AUC for identifying the molecular subgroups of high-grade glioma reached 0.904, with mean sensitivity of 83.3%, mean specificity of 85.0%, mean accuracy of 83.3%, and mean time expense of 10.6 s. The deep learning model performed better than PCA-SVM model and UMAP model in our dataset. At last, tumor-associated biomolecules (e.g. nucleic acid, tyrosine, tryptophan, cholesteryl ester, fatty acid, and collagen) were found to significantly contribute to the accurate molecular subgrouping. Our accurate and rapid Raman molecular subgrouping may facilitate optimal surgical resection and instant post-operative decision-making.

First, our AI-assisted Raman platform for rapid and accurate molecular subgrouping of high-grade glioma may improve prognosis. For the treatment of high-grade glioma, surgery as safely feasible followed by involved-field radiotherapy plus concomitant and maintenance temozolomide chemotherapy define the standard of care since 2005 (42). Nonetheless, determining the optimal extent of surgical resection during operation remains a formidable challenge, and that is crucial for enhancing the prognostic outlook of individuals afflicted with high-grade gliomas. Molecular alterations have been shown to correlate with the prognosis of patients diagnosed with high-grade glioma, such as the mutation status of IDH and the methylated status of MGMT (43, 44). According to the findings of a recent study, the overall survival (OS) was observed to be significantly longer with increasing extent of resection (EOR) in MGMT methylated tumors. Similarly, progression-free survival (PFS) also showed significant differences between residual volume strata in MGMT methylated tumors, while no such trend was observed in MGMT unmethylated tumors (45). Furthermore, younger patients with IDH wildtype tumors who underwent aggressive resection of both contrast-enhanced (CE) and noncontrast-enhanced (NCE) tumors had a survival outcome similar to that of patients with IDH-mutant tumors. However, among younger patients with IDH wildtype tumors who had reduced CE tumors but residual NCE tumors, the survival outcome was worse. In contrast, older patients with IDH wildtype tumors benefited from reducing the CE tumor (46). Collectively, surgical goals should be tailored based on molecular subgroups (47, 48). Our AI-assisted Raman platform of molecular subgrouping could be done accurately during surgery, which may facilitate intraoperative decision-making of the optimal extent of surgical resection and so improve prognosis.

Second, our Raman spectroscopy-based method is superior over current intraoperative diagnostic methods of gliomas for molecular subgrouping. Compared with other techniques for intraoperative glioma diagnosis, including ultrasound (49) (US), optical coherence tomography (50) (OCT) and confocal fluorescence microscopy (51) (CFM) which provide structural information in real time, Raman spectroscopy provides molecular information from glioma tissue (28), allowing it to subgroup molecular alterations accurately. Intraoperative US show the ability to margin deep seated brain tumors from normal brain (49). Intraoperative OCT has been able to distinguish high-density/low-density cancer in nine patients with high-grade gliomas (50). Intraoperative confocal microscopy has shown evidence for invasion detection using fluorescence in grades 1 to 2 glioma on 10 patients (51). However, no evidence indicates these modalities could investigate molecular subgroups. In this study, we not only demonstrate that our Raman spectroscopy-based method could achieve accurate and rapid molecular subgrouping but also show that this method is biologically explainable. The specific Raman features corresponding to the tumor-associated biomolecules were found to contribute to the accurate molecular subgrouping. For instance, the reduction of lipid and collagen reflects IDH wild, which is consistent with previous mechanistic studies. Moreover, the discovered

molecular signatures by Raman spectroscopy may help to improve the understanding of the pathological mechanism of glioma in the future.

Regarding Raman-based technology, stimulated Raman spectroscopy (SRS) providing both structural and molecular information has recently shown the possibility of molecular subgrouping of gliomas (31). Deep learning method was used to integrate both structural and molecular information for good subgrouping performance. Nevertheless, current clinical molecular subgrouping of gliomas is on patient level, which actually only uses the core areas of the tumor tissues for detection. Therefore, the spatial distribution of molecular subgrouping is of limited significance for current clinical treatment and may take extra time that is actually very precious during surgery. Additionally, SRS microscopy requires sophisticated and expensive system. Together, Raman fiber-optic spectroscopy may be more suitable for intraoperative glioma molecular subgrouping scenarios.

Unfortunately, our model failed to reach such accuracy and AUC for subgrouping MGMT, TERT, EGFR, Chromosome 7/10 and CDKN2A/B upon our external validation. The decreased performance in 1p/19q, MGMT, and Chromosome 7/10 subgrouping may be due to data imbalance (as shown in Table S1). The decreased performance in MGMT, TERT, and EGFR may be due to the small metabolic differences between molecular subgroups (as shown in Fig. 3). The decreased performance in 1p/19q, MGMT, TERT, CDKN2A/B may be due to the instability of subgrouping (as shown by the larger standard deviation of shadow area in Fig. 4, which may be due to the large intra group difference in each subgroup). To address these issues, several methods could be employed: (i) employ alternative methods to solve the data imbalance issues instead of random oversampling. For example, synthetic minority oversampling technique and algorithmic approaches like cost-sensitive learning helps in preserving the original distribution and reduces the risk of overfitting. (ii) Apply more advanced preprocessing algorithms to improve classification accuracy, such as spectral preprocessing methods based on deep learning (52). (iii) Adjust the architecture and hyperparameters of the model to improve its suitability for spectral classification. For example, increase the number of layers or nodes in the network, and support the optimization of the network by increasing sufficient data volume. (iv) Utilize generative network models such as generative adversarial network for data augmentation (53).

Finally, our method has the potential for in vivo molecular subgrouping of gliomas. Although we do not implement in vivo molecular subgrouping detection, previous researches have demonstrated the solid foundation of in vivo Raman spectroscopy (13, 54, 55). For instance, Michael et al. (54) developed a handheld contact Raman spectroscopy probe technique for live, local detection of cancer cells in the human brain with a sensitivity of 93% and a specificity of 91%. Zhang et al. (23) investigated human glioma using a portable visible resonance Raman analyzer under quasiclinical conditions with over 80% accuracy. Kevin et al. (55) for the first time developed a Raman spectroscopy guidance system in human in vivo integrated with a brain biopsy needle. Future studies that integrate in vivo diagnosis and molecular subgrouping will have great clinical significance and impact on glioma treatment and prognosis.

Methods

Tissue specimen

This study was approved by the Institutional Review Boards of Beihang University and Beijing Tiantan Hospital. The informed consent was obtained from all participants. This study included 7 astrocytoma, 8 oligodendroglioma, and 29 GBM. The enrolled patients' data, including basic demographic information, imaging data, pathological diagnosis, and molecular characteristics were collected from the hospital information system. Before the operation, every patient underwent enhanced MRI, including T1-weighted, T1-contrast, T2-weighted, and T2-Flair (T2-fluid-attenuated inversion recovery) modalities. Two experienced neuroradiologists independently reviewed the MRI data of patients, and those diagnosed with high-grade glioma were considered for further analysis. For tissue collection during the operation, tumor tissues from patients diagnosed with high-grade glioma based on preoperative MRI were validated using rapid intraoperative tissue pathology. Only specimens showing tissue pathology consistent with the MRI images were collected. After the tumor tissue was resected, a sodium chloride solution was used to remove blood adhered to the tumor tissue. The original tumor tissue was then cut into 2–5 small tissue particles (approximately 2 mm × 2 mm × 2 mm). Then, the tumor samples were snap-frozen in liquid nitrogen and stored at −80°C. All procedures were completed within 30 min. The tissues were sectioned and stained with hematoxylin–eosin (H&E) to confirm the pathological diagnosis of each sample. Finally, the tissues prepared on aluminum foil were used for Raman spectroscopic studies.

Next-generation sequencing

The integrated diagnosis of tumors in this study relied on histological pathology and molecular features. The following key molecular features, which contribute to the integrated diagnosis of glioma, were determined using pyrosequencing and/or next-generation sequencing, including the mutation status of IDH1 and IDH2, MGMT promoter methylation status, 1p/19q codeletion status, the mutation status of the TERT promoter, EGFR amplification status, gain of chromosome 7 and loss of chromosome 10, and the homozygous deletion status of CDKN2A/B. Genomic DNA was extracted from frozen tumor tissues using the QIAamp DNA Mini Kit (Qiagen) following the manufacturer's prescribed procedure. The concentration and quality of the DNA were assessed using the Nano-Drop ND-1000 spectrophotometer (NanoDrop Technologies, Houston, TX, USA). Subsequently, 100 ng of the extracted DNA was employed for bisulfite conversion, utilizing the Epitect Bisulfite Kit (Qiagen) in accordance with the manufacturer's instructions (56, 57). RNA was isolated from the frozen tissue sample, and the RNA-seq library was prepared and then subjected to sequencing on the Illumina HiSeq 2000 platform (Illumina, San Diego, CA, USA) employing a 101-bp paired-end sequencing approach (58). IDH mutation status was directly determined through pyrosequencing targeting the IDH1 R132 and IDH2 R172 hotspot regions. Additionally, pyrosequencing was employed to assess methylation within the MGMT promoter region (59). According to WHO CNS5, common diffuse gliomas in adults are divided into three types: astrocytoma, IDH-mutant; oligodendroglioma, IDH-mutant and 1p/19q co-deleted; and glioblastoma, IDH wildtype.

Fiber-optic Raman spectroscopy

The Raman spectroscopy system is composed of Raman probe with filters (RamanProbe, Inphotonics Inc.), 785 nm laser (o8NLDM, Cobolt Inc.), and high-sensitive spectrometer with ddpCCD (Acton 785, Princeton Instrumentation Inc.) (Fig. S1). The numerical aperture (NA) of the Raman probe (1 cm in diameter) is 0.22. The laser excitation power on the tissue was 65 mW

and the exposure time of single spectrum was around 5 s. According to Monte Carlo simulation, the light irradiance is 0.998 W/cm^2, less than the American National Standards Institute limit set out for a 785-nm laser beam.

Raman spectrum preprocessing

The original Raman spectra contain various types of noise and auto-fluorescence background; therefore, the spectra need to be processed before being input into the deep learning model. The preprocessing took four steps: (i) wavenumber selection; (ii) background subtraction; (iii) smoothing; (iv) normalization. In brief, the wavenumber between 400 and 1800 cm^{-1} was selected as the region of interest. The asymmetric least-squares method was applied to subtract the background signal. The data were then smoothed by a Savitzky-Golay filter to reduce the noise and increase the signal-to-noise ratio. The spectra have been preprocessed with iterative multipolynomial fitting, s–g filter, and min–max normalization. For each paired subgroups, the difference spectrum was calculated by vector subtraction between the mean spectra of each subgroup. All the processing mentioned above was done by Python 3.7 library scipy 1.8.0.

Classification model for molecular subgrouping

Using PCA, we assumed that all meaningful information is contained within the variance. Through finding the maximum variance space, we could get principal components (PC1, PC2, etc.) of Raman shifts with high variance. Using SVM, we created a hyper plane ($\omega^* x - b = 0$) with minimum distance between points. SVM method only focuses on class weight from extreme points, in the meanwhile ignoring distances between other points to hyper plane. Therefore, SVM may fit well with Raman spectral data of small sample size. Combing PCA and SVM, we built a machine learning-based classification model for molecular subgrouping of high-grade glioma. All the processing mentioned above was done by Python 3.7 library sklearn 0.24.2.

Different from PCA, UMAP used nonlinear dimensional reduction and found a representation (UMAP1, UMAP2 etc.) of Raman data in low-dimensional space R^N. Firstly, a good map from Riemannian manifold M to R^N was found. Then Raman data D were uniformly drawn from M. By simulating approximate distances in M between points in D that were close enough in R^N, we finally got UMAP values in R^N. Here, we built supervised UMAP classification model for molecular subgrouping of high-grade glioma. All the processing mentioned above was done by Python 3.7 library UMAP-learn 0.5.3.

Structure of ResNet was described in Fig. 2b. Here, we optimized the 1D ResNet networks for Raman data modeling using the following strategies. (i) In order to achieve the capture of information at different scales, multilayer convolution operations were used. (ii) To simulate many different data patterns, nonlinear activation functions *Tanh* were used instead of *Linear* or *Relu*. (iii) To achieve accurate optimization of hyper parameters of network, backpropagation and gradient descent were used to fit spectral wavenumber information. (iv) The saliency map of deep learning models (ResNet) was simulated by the binary stochastic filtering (BSF) feature selection methods (32). Accuracy and cross-entropy loss are two indicators that are often used to assess the performance and reliability of CNN models. With learning iterations, the accuracy and cross-entropy loss curves of the validation set gradually tend to converge, indicating that the model is not over-fitting. All the processing mentioned above was done by Python 3.7 Library keras 2.2.4 and tensorflow 1.14.0.

Model evaluation

For subgrouping evaluation in each molecular alteration, IDH mutation, 1p/19q codeletion, MGMT methylation, TERT mutation, EGFR amplification, chromosome +7/−10, and CDKN2A/B homozygous deletion were defined as positives labels. The accuracy together with the sensitivity and specificity of the binary classification models were calculated using a testing dataset from extra samples, which avoids spectra from the same samples for train and test set. Outcomes of high-grade glioma Raman classification were evaluated with respect to sensitivity (SEN), specificity (SPC), and accuracy (ACC) as follows:

$$\text{Sensitivity} = \frac{\text{True positive}}{\text{True positive} + \text{False negative}} \quad (1)$$

$$\text{Specificity} = \frac{\text{True negative}}{\text{True negative} + \text{False postive}} \quad (2)$$

$$\text{Accuracy} = \frac{\text{True negative} + \text{True positive}}{\text{True negative} + \text{True positive} + \text{False postive} + \text{False negative}}. \quad (3)$$

True positives mean correct positive labels of prediction (IDH mutation, 1p/19q codeletion, MGMT methylation, TERT mutation, EGFR amplification, Chromosome +7/−10, and CDKN2A/B homozygous deletion). True negatives mean correct negative labels of prediction. False positives mean false positive labels of prediction. False negatives mean false negative labels of prediction.

The binary classification for glioma molecular subgrouping was evaluated with a binary receiver operating characteristic (ROC) analysis according to the method. We employed the roc_ curve function from Scikit-learn (version 0.21.3) in Python to produce the ROC curve. This curve was generated by continuously adjusting the probability threshold for each category, based on the ground truth. These probabilities are predictions from the classification model, whereas the ground truth derives from clinical pathological diagnoses confirmed by pyrosequencing and next-generation sequencing. The AUC, which ranges from 0 to 1, assesses the model's capability to distinguish between different glioma subgroups with utmost sensitivity and specificity.

Supplementary Material

Supplementary material is available at *PNAS Nexus* online.

Funding

This work was supported by National Natural Science Foundation of China (No. U23B2046, No. 81930048, No. 62027824, and No. 62205010); National Key R&D Program of China (No. 2022YFC 2403905); Beijing Natural Science Foundation (No. 7224367 and No. L223018); Capital Health Research and Development of Special (No. 2022-2-2047); Fundamental Research Funds for the Central Universities (No. YWF-22-L-547 and No. YWF-22-L-1265).

Author Contributions

C.L., J.W., and J.S. contribute equally. S.Y. and N.J. supervised the project. S.Y., X.C., and N.J. designed the methodology. N.J. and J.W. provided glioma tissue specimens and RNA sequencing results. C.L. and J.W. performed Raman spectral acquisition experiments. C.L. and J.S. processed the data. C.L., X.C., J.W., S.Y., and N.J. wrote

the manuscript. All authors edited the manuscript. S.Y. and N.J. finalized and approved the manuscript.

Preprint

This manuscript was posted on a preprint on medRxiv: (DOI: https://doi.org/10.1101/2023.07.03.23292176).

Data Availability

Data and code are publicly available via Zenodo (https://zenodo.org/records/11229959). The main data supporting the findings of this study are available within the article and its Supplementary Information. The system control software and the data collection software are proprietary and used in licensed technologies.

References

1 Lapointe S, Perry A, Butowski NA. 2018. Primary brain tumours in adults. *Lancet*. 392:432–446.
2 Stupp R, Lukas RV, Hegi ME. 2019. Improving survival in molecularly selected glioblastoma. *Lancet*. 393:615–617.
3 Brown TJ, *et al.* 2016. Association of the extent of resection with survival in glioblastoma: a systematic review and meta-analysis. *JAMA Oncol*. 2:1460–1469.
4 Wijnenga MMJ, *et al.* 2018. The impact of surgery in molecularly defined low-grade glioma: an integrated clinical, radiological, and molecular analysis. *Neuro Oncol*. 20:103–112.
5 Butterfield JT, *et al.* 2022. Racial disparities in recommendations for surgical resection of primary brain tumours: a registry-based cohort analysis. *Lancet*. 400:2063–2073.
6 Chaligne R, *et al.* 2021. Epigenetic encoding, heritability and plasticity of glioma transcriptional cell states. *Nat Genet*. 53:1469–1479.
7 Tan Y, *et al.* 2019. A radiomics nomogram may improve the prediction of IDH genotype for astrocytoma before surgery. *Eur Radiol*. 29:3325–3337.
8 MacIver CL, *et al.* 2021. Filtration-histogram based magnetic resonance texture analysis (MRTA) for the distinction of primary central nervous system lymphoma and glioblastoma. *J Pers Med*. 11:876.
9 Jiang C, *et al.* 2019. Fusion radiomics features from conventional MRI predict MGMT promoter methylation status in lower grade gliomas. *Eur J Radiol*. 121:108714.
10 Lu C-F, *et al.* 2018. Machine learning-based radiomics for molecular subtyping of gliomas. *Clin Cancer Res*. 24:4429–4436.
11 Reinges MHT, *et al.* 2004. Course of brain shift during microsurgical resection of supratentorial cerebral lesions: limits of conventional neuronavigation. *Acta Neurochir (Wien)*. 146:369–377; discussion 377.
12 Ganser KA, *et al.* 1997. Quantification of brain shift effects in MRI images. *Biomed Tech (Berl)*. 42:247–248.
13 Jermyn M, *et al.* 2015. Intraoperative brain cancer detection with Raman spectroscopy in humans. *Sci Transl Med*. 7:274ra19.
14 Huang Z, Zeng H, Hamzavi I, McLean DI, Lui H. 2001. Rapid near-infrared Raman spectroscopy system for real-time in vivo skin measurements. *Opt Lett*. 26:1782–1784.
15 Huang Z, *et al.* 2003. Near-infrared Raman spectroscopy for optical diagnosis of lung cancer. *Int J Cancer*. 107:1047–1052.
16 Bergholt MS, *et al.* 2011. In vivo diagnosis of esophageal cancer using image-guided Raman endoscopy and biomolecular modeling. *Technol Cancer Res Treat*. 10:103–112.
17 Lin K, Zheng W, Lim CM, Huang Z. 2017. Real-time in vivo diagnosis of nasopharyngeal carcinoma using rapid fiber-optic Raman spectroscopy. *Theranostics*. 7:3517–3526.
18 Shu C, Zheng W, Lin K, Lim C, Huang Z. 2021. Label-free follow-up surveying of post-treatment efficacy and recurrence in nasopharyngeal carcinoma patients with fiberoptic Raman endoscopy. *Anal Chem*. 93:2053–2061.
19 Shu C, *et al.* 2021. Deep learning-guided fiberoptic Raman spectroscopy enables real-time in vivo diagnosis and assessment of nasopharyngeal carcinoma and post-treatment efficacy during endoscopy. *Anal Chem*. 93:10898–10906.
20 Žuvela P, *et al.* 2019. Fiber-optic Raman spectroscopy with nature-inspired genetic algorithms enhances real-time in vivo detection and diagnosis of nasopharyngeal carcinoma. *Anal Chem*. 91:8101–8108.
21 Qi Y, Liu Y, Luo J. 2023. Recent application of Raman spectroscopy in tumor diagnosis: from conventional methods to artificial intelligence fusion. *PhotoniX*. 4:22.
22 Qi Y, *et al.* 2022. High-precision intelligent cancer diagnosis method: 2D Raman figures combined with deep learning. *Anal Chem*. 94:6491–6501.
23 Zhang L, *et al.* 2023. A handheld visible resonance Raman analyzer used in intraoperative detection of human glioma. *Cancers (Basel)*. 15:1752.
24 Wu B, *et al.* 2020. Glioma tumors classified using visible resonance Raman spectroscopy and machine learning. In: Lee B, Mazzali C, Corwin K, Jason Jones R, editors. *Frontiers in optics/Laser science*. Washington (DC): Optica Publishing Group. p. JW6A.17.
25 Zhou Y, *et al.* 2019. Optical biopsy identification and grading of gliomas using label-free visible resonance Raman spectroscopy. *J Biomed Opt*. 24:1–12.
26 Livermore LJ, *et al.* 2020. Raman spectroscopy to differentiate between fresh tissue samples of glioma and normal brain: a comparison with 5-ala-induced fluorescence-guided surgery. *J Neurosurg*. 135:469–479.
27 Riva M, *et al.* 2021. Glioma biopsies classification using Raman spectroscopy and machine learning models on fresh tissue samples. *Cancers (Basel)*. 13:1073.
28 Galli R, *et al.* 2019. Rapid label-free analysis of brain tumor biopsies by near infrared Raman and fluorescence spectroscopy—a study of 209 patients. *Front Oncol*. 9:1165.
29 Uckermann O, *et al.* 2018. IDH1 mutation in human glioma induces chemical alterations that are amenable to optical Raman spectroscopy. *J Neurooncol*. 139:261–268.
30 Sciortino T, *et al.* 2021. Raman spectroscopy and machine learning for IDH genotyping of unprocessed glioma biopsies. *Cancers (Basel)*. 13:4196.
31 Hollon T, *et al.* 2023. Artificial-intelligence-based molecular classification of diffuse gliomas using rapid, label-free optical imaging. *Nat Med*. 29:828–832.
32 Trelin, A, Prochazka, A. Binary stochastic filtering: a method for neural network size minimization and supervised feature selection. bioRxiv 04510. https://doi.org/10.48550/arXiv.1902.04510, preprint: not peer reviewed.
33 Dukor RK. 2001. Vibrational spectroscopy in the detection of cancer. In: Chalmers JM, Griffiths PR, editors. *Handbook of vibrational spectroscopy*. John Wiley & Sons, Ltd.
34 Movasaghi Z, Rehman S, Rehman IU. 2007. Raman spectroscopy of biological tissues. *Appl Spectrosc Rev*. 42:493–541.
35 Ye J, *et al.* 2017. Idh1 deficiency attenuates gluconeogenesis in mouse liver by impairing amino acid utilization. *Proc Natl Acad Sci USA*. 114:292–297.

36 Bauchle CJ, *et al.* 2021. Mitochondrial efflux of citrate and isocitrate is fully dispensable for glucose-stimulated insulin secretion and pancreatic islet **B**-cell function. *Diabetes*. 70:1717–1728.

37 Branzoli F, *et al.* 2019. Cystathionine as a marker for 1p/19q codeleted gliomas by in vivo magnetic resonance spectroscopy. *Neuro-Oncol*. 21:765–774.

38 Wang N, Wang J, Wang P, Ji N, Yue S. 2023. Label-free Raman spectromicroscopy unravels the relationship between MGMT methylation and intracellular lipid accumulation in glioblastoma. *Anal Chem*. 95:11567–11571.

39 Li N, *et al.* 2021. Liquid chromatography-mass spectrometry based metabolic characterization of pleural effusion in patients with acquired EGFR-TKI resistance. *J Pharm Biomed Anal*. 202: 114147.

40 Seldin M, *et al.* 1994. Glycogen-synthase—a putative locus for diet-induced hyperglycemia. *J Clin Invest*. 94:269–276.

41 Minami JK, *et al.* 2023. *CDKN2A* deletion remodels lipid metabolism to prime glioblastoma for ferroptosis. *Cancer Cell*. 41:1048.

42 Le Rhun E, *et al.* 2019. Molecular targeted therapy of glioblastoma. *Cancer Treat Rev*. 80:101896.

43 Reuss DE. 2023. Updates on the WHO diagnosis of IDH-mutant glioma. *J Neurooncol*. 162:461–469.

44 Butler M, *et al.* 2020. MGMT status as a clinical biomarker in glioblastoma. *Trends Cancer*. 6:380–391.

45 Gerritsen JKW, *et al.* 2023. Impact of maximal extent of resection on postoperative deficits, patient functioning, and survival within clinically important glioblastoma subgroups. *Neuro Oncol*. 25: 958–972.

46 Molinaro AM, *et al.* 2020. Association of maximal extent of resection of contrast-enhanced and non-contrast-enhanced tumor with survival within molecular subgroups of patients with newly diagnosed glioblastoma. *JAMA Oncol*. 6:495–503.

47 Drexler R, *et al.* 2023. DNA methylation subclasses predict the benefit from gross total tumor resection in IDH-wildtype glioblastoma patients. *Neuro Oncol*. 25:315–325.

48 Hervey-Jumper SL, *et al.* 2023. Interactive effects of molecular, therapeutic, and patient factors on outcome of diffuse low-grade glioma. *J Clin Oncol*. 41:2029–2042.

49 Regelsberger J, Lohmann F, Helmke K, Westphal M. 2000. Ultrasound-guided surgery of deep seated brain lesions. *Eur J Ultrasound*. 12:115–121.

50 Böhringer HJ, *et al.* 2009. Imaging of human brain tumor tissue by near-infrared laser coherence tomography. *Acta Neurochir (Wien)*. 151:507–517; Discussion 517.

51 Sanai N, *et al.* 2011. Intraoperative confocal microscopy in the visualization of 5-aminolevulinic acid fluorescence in low-grade gliomas. *J Neurosurg*. 115:740–748.

52 Hu J, *et al.* 2024. RSPSSL: a novel high-fidelity Raman spectral preprocessing scheme to enhance biomedical applications and chemical resolution visualization. *Light: Sci Appl*. 13:52.

53 Wu M, *et al.* 2021. Deep learning data augmentation for Raman spectroscopy cancer tissue classification. *Sci Rep*. 11:23842.

54 Desroches J, *et al.* 2018. A new method using Raman spectroscopy for in vivo targeted brain cancer tissue biopsy. *Sci Rep*. 8:1792.

55 Desroches J, *et al.* 2019. Development and first in-human use of a Raman spectroscopy guidance system integrated with a brain biopsy needle. *J Biophotonics*. 12:e201800396.

56 Zhang C-B, *et al.* 2014. Correlation of Idh1/2 mutation with clinicopathologic factors and prognosis in anaplastic gliomas: a report of 203 patients from China. *J Cancer Res Clin Oncol*. 140:45–51.

57 Chai R-C, *et al.* 2019. A novel analytical model of MGMT methylation pyrosequencing offers improved predictive performance in patients with gliomas. *Mod Pathol*. 32:4–15.

58 Chai R-C, *et al.* 2019. Combinations of four or more CPGS methylation present equivalent predictive value for *mgmt* expression and temozolomide therapeutic prognosis in gliomas. *CNS Neurosci Ther*. 25:314–322.

59 Zhang K, *et al.* 2022. Clinical management and survival outcomes of patients with different molecular subtypes of diffuse gliomas in China (2011–2017): a multicenter retrospective study from CGGA. *Cancer Biol Med*. 19:1460–1476.